



Reducing high-temperature corrosion on high-alloyed stainless steel superheaters by co-combustion of municipal sewage sludge in a fluidised bed boiler



Sofia Karlsson^{a,*}, Lars-Erik Åmand^b, Jesper Liske^a

^a Department of Chemical and Biological Engineering, Energy and Materials, Chalmers University of Technology, S-412 96 Göteborg, Sweden

^b Department of Energy and Environment, Chalmers University of Technology, S-412 96 Göteborg, Sweden

HIGHLIGHTS

- Effects of co-firing sewage sludge with biomass/waste in a CFB boiler are studied.
- Burning waste and biofuels results in a corrosive flue gas.
- The corrosivity is mainly due to the presence of alkali chlorides in the fuel gas.
- The addition of digestive sewage sludge decreases corrosion rate significantly.
- The corrosive alkali chlorides will transform to less corrosive alkali compounds.

ARTICLE INFO

Article history:

Received 5 June 2014

Received in revised form 1 September 2014

Accepted 3 September 2014

Available online 16 September 2014

Keywords:

Alkali chlorides

Corrosion

Co-combustion

Fluidised bed boiler

Municipal sewage sludge

ABSTRACT

One way of mitigating alkali chloride induced corrosion in biomass and waste-fired boilers is by using additives or by co-combustion and thereby decreasing the corrosiveness of the flue gas and deposits. The effect of co-firing digested sewage sludge with a mixture of biomass and waste (78% bark pellets + 22% Solid Recovered Fuel, denoted “SRF”) was investigated in a 12 MW circulating fluidised bed (CFB) boiler. The initial corrosion attack of the stainless steel 304L at 600 °C (material temperature) was investigated during 24 h exposures. The exposures were carried out in the flue gas environment from three fuel-mixes: SRF, MSS1-low (SRF with municipal sewage sludge, low dosage) and MSS2-high (SRF with municipal sewage sludge, high dosage). The results showed that the most severe corrosion attack on 304L occurred without sewage sludge in the SRF exposure. This attack was characterised by a corrosion product layer up to 100 µm in thickness and signs of internal corrosion of the steel. The deposit in the SRF case was dominated by alkali chlorides. The exposures with co-combustion of sewage sludge, MSS1-low and MSS2-high, showed a significant decrease in corrosion. The steel sample of 304L performed especially well in the latter case when it was protected by a thin oxide of less than 0.3 µm in thickness. This deposit was dominated by sulphate- and phosphate-containing compounds but traces of aluminium silicate compounds were also found. Furthermore, the concentration of alkali chlorides was low. Thus, the initial corrosion attack was greatly reduced by co-combustion of digested sewage sludge with SRF.

© 2014 The Authors. Published by Elsevier Ltd. This is an open access article under the CC BY-NC-ND license (<http://creativecommons.org/licenses/by-nc-nd/3.0/>).

1. Introduction

The production of electricity from renewable energy sources, such as waste and biofuels, is presently on the increase throughout the world. Being renewable, these fuels are not considered to make any net contribution of carbon dioxide (CO₂) to the atmosphere when combusted. However, these fuels usually contain large

amounts of alkali chloride which result in a very corrosive flue gas. In contrast, the sulphur dioxide (SO₂) content is typically low [1–4]. Hence, the deposits formed on the superheater tubes are often rich in alkali chlorides (potassium chloride (KCl) and sodium chloride (NaCl)) and it has been shown that high temperature corrosion of stainless steels is greatly enhanced by the presence of alkali chlorides [5–14]. The corrosion rates of the superheaters in a boiler can be reduced by keeping the steam temperature low. However, this results in poor electrical efficiency. The steam parameters can be maintained at high temperature

* Corresponding author.

E-mail addresses: sofia.karlsson@chalmers.se (S. Karlsson), lars-erik.amand@chalmers.se (L.-E. Åmand), jesper.liske@chalmers.se (J. Liske).

and pressure if the high temperature corrosion is prevented. The strategies to prevent high temperature corrosion include co-combustion, additives and more advanced superheater materials or higher alloyed superheater materials.

One of the explanations for the corrosive behaviour of alkali chlorides towards stainless steels is the formation of alkali chromates. It has been shown that alkali chlorides react with chromium (Cr) in the initially formed protective oxide on stainless steel, forming alkali chromates [6,7,9,10,15–17]. This results in a chromium depleted oxide which is then converted into an iron-rich fast-growing oxide. This oxide has much poorer protective properties as it has higher diffusion rates compared to chromium rich oxides. This reaction scheme is also true for potassium carbonate (K_2CO_3), which reacts with protective oxide forming potassium chromate (K_2CrO_4) and $CO_2(g)$ [16,18]. Thus, the chromate formation reaction is not limited solely to alkali chlorides. After the breakdown of the initially protective oxide, the iron-rich oxide formed after reaction with alkali compounds is susceptible to chlorine-induced corrosion by chlorine ions penetrating the oxide scale. This leads to the formation of transition metal chlorides (e.g. iron chloride ($FeCl_2$)) at the metal/oxide interface causing poor scale adherence.

Another explanation for the accelerated corrosion attack is the active oxidation mechanism, initially proposed by McNallan [19,20] and further developed by Grabke [5]. In this mechanism, it is suggested that chlorine ($Cl_2(g)$) diffuses through micro cracks and pores in the oxide scale, forming volatile metal chlorides in the reducing environment at the oxide/metal interface. The gaseous metal chlorides then diffuse through the oxide, forming metal oxide in the outer part of the scale where the partial pressure of oxygen is higher, releasing $Cl_2(g)$. The molecular chlorine formed in this way has been suggested to diffuse inwards through the scale, to react with the metal again.

In order to mitigate the corrosion in waste and biomass-fired boilers, fuel additives can be used for altering the corrosive environment and thus restricting the corrosion attack. The fact that the flue gas chemistry can be altered by means of fuel additives or co-combustion has also been demonstrated in several papers [3,15,21–33] and the effect on the corrosion attack has also been evaluated [15,22,23,26–29]. In biomass and waste-fired boilers, the additives or co-combustion has mainly focused on increasing the availability of sulphur (in the form of SO_2 and/or SO_3) in the boiler. This includes sulphur-based additives such as elemental sulphur (S) [15,22,24,25,28] and ammonium sulphate ($(NH_4)SO_4$) [24–26,29], sulphur recirculation [27] or by co-combustion of waste and biomass with coal, peat and municipal sewage sludge [21,23,26,30–33]. The main aim of using these additives (or co-combustion) was to sulphate alkali chlorides into their corresponding sulphates during the simultaneous release of hydrogen chloride (HCl) or Cl_2 . Laboratory studies have shown that the presence of potassium sulphate (K_2SO_4) induces no accelerated corrosion attack on stainless steels at 600 °C [18]. The non-corrosive nature of K_2SO_4 at this temperature is explained by its reluctance to react with the protective, chromium-rich oxide form K_2CrO_4 . Thus, the corrosion properties of the stainless steel remain intact.

In addition to decreasing the presence of alkali chlorides by sulphation, other measures have been taken [34]. By means of co-combustion of biomass/waste with sewage sludge, several reactions with alkali can occur. This includes, for instance, converting the alkali chlorides into alkali sulphates, alkali phosphates or by binding the alkali part of alkali chlorides to aluminium silicates. In contrast to alkali chlorides, they do not deplete the protective oxide in chromium by forming K_2CrO_4 . In this study, two different municipal sewage sludges were tested as co-fuels at the 12 MW_{th} CFB boiler on Chalmers campus. The focus lies on the initial corrosion attack of the stainless steel 304L and how these additives can mitigate the corrosive nature of the reference fuel (Solid Recovered

Fuel and Bark). Special attention is paid to the presence of S, phosphorus (P), calcium (Ca) and aluminium silicates in the deposits formed on the corrosion probe used and their ability to react with alkali chlorides in order to converting the alkali chlorides into less corrosive compounds.

2. Experimental

2.1. Research boiler, fuels and boiler operating conditions

The experiments were performed in the 12 MW_{th} circulating fluidised bed (CFB) boiler, located at Chalmers University of Technology, shown in Fig. 1. The combustion chamber (1) has a cross section of 2.25 m² and a height of 13.6 m. The various fuels are fed to the bottom of the bed through a fuel feed chute (2). The circulating material is separated at a primary cyclone (5) and returned to the combustion chamber through the cyclone leg and loop seal. An external heat exchanger cools the circulating material before re-entering the combustion chamber when required. Primary air is introduced through air nozzles located at the bottom of the riser and secondary air 2.1 m above the bottom plate (4). The exhaust gas is cooled to 150 °C in the convection pass. Effective soot blowers (using steam blown probes) are installed along each section of the convection pass. These soot blowers are regularly used to keep the flue gas temperature below 180 °C (once or twice every 24 h). Fly ashes are separated in the secondary cyclone (8) and the textile filter (9). Silica sand ($dp = 0.3$ mm) was used as bed material in all cases. The operating conditions presented in Table 1 are typical of a commercially operated CFB boiler. This means a fluidising velocity between 5 and 6 m/s in the top of the riser that leads to a proper circulation of bed material through the primary cyclone, good heat transfer of moving bed particles and an attrition of the fuel ash into fly ash, which is important in order to avoid accumulation of bottom bed ash. Other typical operating conditions are proper excess air ratio (20–25% excess air) and a bottom bed temperature of 850 °C.

Three combustion cases were investigated and their corresponding operating conditions are presented in Table 1. First, case *SRF* in which bark pellets were co-fired with waste (Solid Recovered Fuel) pellets produced by IcoPower in the Netherlands. The share of waste was 22% based on the total amount of dry fuel supplied to the boiler. The bark was crushed, dried and pressed into pellets. Secondly, case *MSS1-low* with additional combustion to the case *SRF* of municipal sewage sludge from a waste water treatment plant named Sjölundaverket with a mixture of 7.3%. Sjölundaverket takes care of sewage waste water from the city of Malmö in Sweden. Thirdly, case *MSS2-high* with additional combustion to the case *SRF* of municipal sewage sludge from a waste water treatment plant named Himmerfjärdsverket with a mixture of 13%. Himmerfjärdsverket takes care of sewage waste water from the city of Södertälje and the south-west part of Stockholm.

The element compositions of the separate fuels are given in Table 2. The main difference in composition is high chlorine content in the *SRF* case and the ashes from both *SRF* and bark have a high content of Ca. Moreover, the precipitating agent for P was iron-sulphate (Fe_2SO_4) for both sewage sludges (*MSS1* and *MSS2*), which is reflected by the high iron (Fe) and P content. The digestion of the sludge during which methane (CH_4) is produced leads to a higher ash concentration compared to undigested sludge. After digestion the sludge was mechanically dewatered using high speed centrifuges, lowering the moisture content from 92% to approximately 72–78% and it is difficult to decrease it further without the use of drying equipment. Moisture contents of 72–78% lead to low heating values in the range of 1–2 MJ/kg fuel as supplied to the boiler. These low heating values require a base

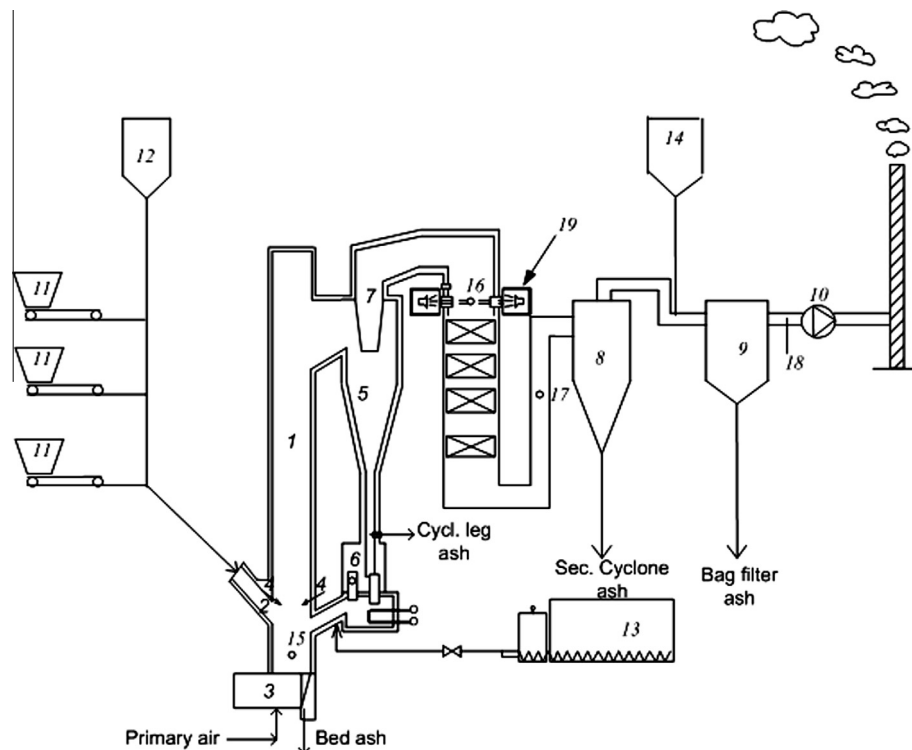


Fig. 1. The 12 MW_{th} FBC boiler at Chalmers University of Technology (1) combustion chamber; (2) fuel feed chute; (3) air plenum; (4) secondary air inlet at 2.1 m; (5) hot primary cyclone; (6) loop seal; (7) cyclone exit duct; (8) cold secondary cyclone; (9) bag house filter; (10) flue gas recirculation fan; (11) fuel bunkers; (12) sand bin; (13) sludge pump; (14) hydrated lime bin; (15) bed ash sampling hole; (16) measurement spot (before convection pass) IACM instrument, deposit probe and FTIR; (17) measurement spot (after convection pass) FTIR; (18) measurement spot (stack) FTIR, (19) IACM instrument.

Table 1
Operating conditions of the boiler for the various test cases.

Test	Unit	SRF	MSS1	MSS2
Load	MW _{th}	6.7	6.5	6.2
Bed temp. (bottom)	°C	847	853	851
Comb. temp. (top)	°C	873	872	873
Comb. temp. after primary cyclone (16) ^a	°C	775	748	746
Flue gas temp. after economiser (17) ^b	°C	177	173	166
Total riser pressure drop	kPa	7.7	7.6	7.4
Excess air ratio	–	1.20	1.20	1.21
Air staging: primary air flow divided by total air flow	%	54	65	66
Superficial velocity at the top of riser	ms ⁻¹	5.9	5.6	4.9
S/Cl molar ratio	–	0.6	1.6	2.0
Cl(Na + K) molar ratio	–	0.4	0.4	0.4

^a At position 16 in Fig. 1.

^b At position 17 in Fig. 1.

load of fuel with higher heating values and the sludge could be largely regarded as an additive. However, the heat used for vaporization of the moisture in the sludge can be recovered by installing a flue gas condenser.

2.2. Measurement equipment in the boiler

The flue gas composition was obtained by conventional instrumentation, (Fourier Transform Infrared Spectroscopy) FTIR instrument, Bomen MB100 and an in-situ alkali chloride monitor (IACM) for the alkali chlorides. Measurements of alkali chlorides (NaCl and KCl) were taken upstream of the convection pass (27) using an IACM. The IACM (Fig. 2) has been used in previous projects at the same boiler and is described in detail by Kassman et al. [25,26].

By using a gas extraction probe at the same position (16) as the IACM, it is possible to control the chlorine in the gas phase in the form of HCl. An air-cooled probe (Fig. 3), equipped with deposit rings, was inserted into the flue gas channel (position (16)). In order to simulate a superheater tube, it was maintained at constant temperatures of 600, 650 and 700 °C during a period of 24 h of exposure to flue gases at 746–775 °C, Table 2. This paper only includes results from the deposit rings exposed at 600 °C.

2.3. Materials investigated

The materials used in this study were the austenitic stainless steels 304L and Sanicro 28. For chemical composition see Table 3. All samples rings had an outer diameter of 38 mm and a width of 15 mm. Prior to exposure the samples were cleaned in acetone

Table 2
Fuel properties.

	Bark	SRF	MSS1-low	MSS2-high
Moisture, %	10	5.2	78	73
Ash, % dry	4.2	13	41	41
Volatiles, % daf	73	88	90	92
<i>Ultimate analysis, % daf</i>				
C	54.3	53.6	53.0	54.4
H	6.1	7.3	7.5	7.8
O	38.6	37.3	29.5	29.0
S	0.03	0.24	3.0	2.4
N	0.50	0.91	6.8	6.2
Cl	0.02	0.62	0.18	0.10
<i>Ash elements g/kg dry ash</i>				
K	46	11	12	11
Na	10	22	7.1	5.0
Al	26	48	50	48
Si	110	138	124	105
Fe	12	18	129	190
Ca	198	192	93	59
Mg	17	11	13	9.9
P	10	5.1	74	78
Ti	1.0	11	4.3	12
Ba	2.9	1.8	1.3	0.6
<i>Lower heating value (H) MJ/kg</i>				
H, daf	20.3	21.1	21.5	22.3
H, raw	16.2	17.3	0.75	1.63

and ethanol using ultrasonic agitation and were then dried with air and stored in plastic bottles. Two rings, 304L and Sanicro 28, were used in every exposure case which lasted for 24 h. The temperature was kept at 600 °C (material temperature) and the samples were stored in a desiccator prior to and after exposure.

2.4. Corrosion product characterisation

After exposure the samples were analysed by means of three analytical methods: Scanning Electron Microscope (SEM) together with energy dispersive X-ray (EDX), X-ray diffraction (XRD) and Ion Chromatography (IC). The 304L sample rings were mounted in epoxy. Afterwards they were cut and polished. The cross section, which included deposit, oxide layer and metal, was then analysed with SEM/EDX. The SEM imaging was performed using an FEI Quanta 200 ESEM FEG. The EDX detector was linked with the SEM and an Oxford Inca EDX system was used for EDX mapping and point analysis. The microscope was operated at 20 kV.

For the Sanicro 28 sample rings, the deposit was mechanically removed and crystalline compounds were analysed with XRD,

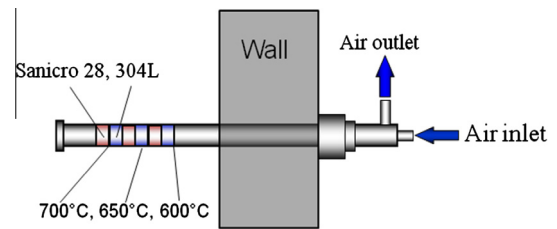


Fig. 3. Schematic image of the air-cooled corrosion probe equipped with sample rings at a surface temperatures of 600, 650 and 700 °C.

Table 3
Chemical composition of the alloys 304L and Sanicro 28.

(Weight%)	Cr	Ni	Mn	Si	Mo	Fe	n_{Cr}/n_{Fe}
304L	19.5	9.6	1.4	1.1	0.3	67.0	0.29
Sanicro 28	27.0	31.0	<2.0	0.6	3.5	34.5	0.78

using a Siemens D5000 powder diffractometer equipped with grazing incidence beam attachment and a Göble mirror. The radiation used was Cu K α and the angle of incident was 2°. The detector measured between 12° < 2 θ < 65°. The XRD results given in Table 4 are divided into three levels with respect to their intensity: weak, medium and strong. These levels are derived from the strongest peak in the diffractogram. Hence, the intensity of the strongest (i.e. highest) peak for each phase was divided by the intensity of the strongest peak in the diffractogram. All values between 1 and 0.3 were denoted strong, 0.3–0.1 medium and <0.1 weak.

After the XRD analysis, the deposit was leached in Milli-Q water for quantification of water soluble anion. The amounts of chlorine (Cl⁻), sulphate (SO₄²⁻) and chromate ions (CrO₄²⁻) were determined using a Dionex ICS-90 Ion Chromatography (IC) system. The anions were analysed with an IonPac AS4A-SC analytic column and 1.8 mM sodium carbonate/1.7 mM sodium bicarbonate was used as an eluent. The flow rate was 2 mL/min and detection limit of the anions is in the sub-ppm range.

3. Results

3.1. Flue gas composition

A study of a transient in the flue gas composition of alkali chlorides (KCl + NaCl), SO₂ and HCl upon starting the co-firing of SRF and sludge gives an insight into the gas phase chemistry surrounding the corrosion probe, Fig. 3, located in measurement hole

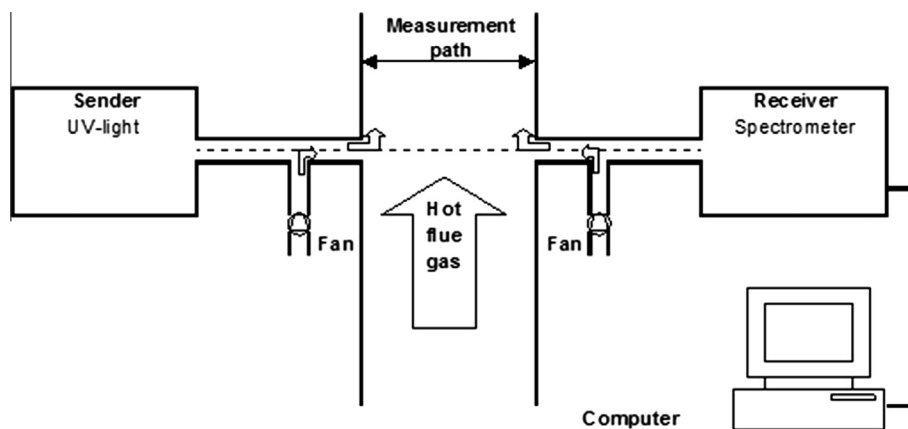


Fig. 2. Schematic view of an in-situ alkali chloride monitor (IACM) installation used at position (16) in Fig. 1.

Table 4

Crystalline phases detected with XRD on deposits formed on Sanicro 28 samples, exposed for 24 h at 600 °C.

	KCl	NaCl	CaSO ₄	K ₂ Ca ₂ (SO ₄) ₃	CaCO ₃	KCaFe(PO ₄) ₂	KAlSi ₂ O ₆
<i>SRF</i>	S	M	W		W		
<i>MSS1-low</i>	S	M	M	M			
<i>MSS2-high</i>			S	M		S	M

S = strong intensity, M = medium intensity, W = weak intensity.

16 in Fig. 1. Such a transient is plotted in Fig. 4. On the x-axis the time is divided into five (I–V) time slots. Alkali chlorides and one of the SO₂ signals is from the IACM (19) in Fig. 1 while the other SO₂ signal, as well as the HCl, originated from the FTIR sampling gas from a position after the convection pass of the boiler ((17) in Fig. 1). Time slot I corresponds to mono-combustion of wood chips only. These wood chips have a low content of alkali elements (K + Na), Cl and S leading to low concentrations of (KCl + NaCl), HCl and SO₂. When substituting the wood chips with bark pellets (period II), the alkali chlorides showed up in the flue gas in a concentration of around 10 ppm, i.e. a level that normally neither causes problems with deposits on superheater tubes nor corrosion even if low alloyed steels are used. During period III, the SRF was gradually increased in four steps up to the level corresponding to test case *SRF*. Both the increased alkali and chlorine loading resulted in a tenfold increase of the concentration of alkali chlorides in the flue gas. Most of the chlorine in the SRF appears to end up as KCl + NaCl and not HCl, showing the affinity of chlorine towards alkali rather than hydrogen. Levels of 100 ppm in previous projects have led to severe problems in the buildup of deposits on the tubes of the convection section with frequent use of the steam-blown soot equipment. Also the pressure buildup in the bag filter caused problems due to plugging with alkali chlorides. The start of the sludge combustion during period V is of particular interest. The alkali chloride concentration dropped like a stone and after a while a breakthrough of both HCl and SO₂ could be measured. The sludge contained more S than the bark and SRF and sulphation of alkali chlorides pushing out the Cl as HCl is most likely an important reaction explaining most of the decline of KCl + NaCl seen in Fig. 4. However other elements in the sludge ash such as aluminium silicates (in the form of zeolites) and P captured the alkali into either potassium/sodium aluminium silicates or calcium potassium/sodium phosphates. By analysing both the deposit rings as well as the fly ashes from the present project, a deeper

understanding of the chemistry behind the advantages of co-firing municipal sewage sludge can be achieved.

The gaseous alkali chlorides, HCl and SO₂ for *SRF*, *MSS1-low* and *MSS2-high* are given in Fig. 5. In the *SRF* exposure, the content of gaseous alkali chlorides (KCl + NaCl) in the flue gas was 96 ppm. By adding sewage sludge the alkali content in the flue gas decreased to 28 ppm in the *MSS1-low* case and to only 3 ppm in the *MSS2-high* case. As the alkali concentration decreased, the chlorine showed up instead as HCl with an increase of HCl from 45 ppm (*SRF* case) to 316 ppm for case *MSS2-high*.

3.2. Optical investigation

Fig. 6 shows the sample rings after 24 h of exposure at 600 °C (material temperature). In the *SRF* case, both 304L and Sanicro 28 are covered by a thick, brownish deposit. The deposit layer formed on 304L appears to be more prone to spallation compared to the deposit formed on Sanicro 28. In the *MSS1-low* case the samples are also covered by a brownish deposit layer. The deposit is dense and adherent and seems to be thinner than in the *SRF* exposure. In the *MSS2-high* case, the samples are covered by a reddish deposit. The deposit on both 304L and Sanicro 28 seems to be thinner than the deposits in the cases *SRF* and *MSS1-low*; metallic luster can be seen through the deposit layer.

3.3. Deposit analysis with XRD and IC

The crystalline phases detected by XRD analysis of the deposit are given in Table 4. According to the XRD analysis, the deposits formed on the *SRF* sample are dominated by KCl and NaCl. In addition, CaCO₃ and CaSO₄ with weak intensity diffraction peaks were detected. The addition of sewage sludge in the *MSS1-low* case did not decrease the intensity from the alkali chlorides; KCl and NaCl were detected with strong and medium intensity diffraction peaks

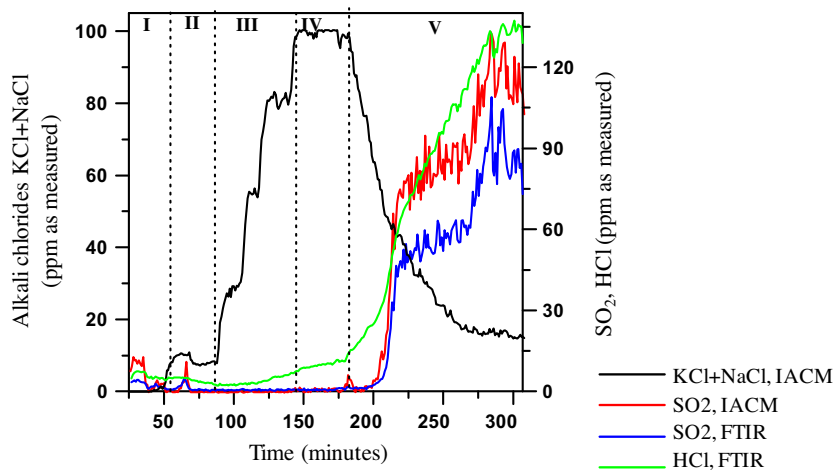


Fig. 4. Alkali chlorides (KCl + NaCl), SO₂ and HCl in transient tests of the introduction of SRF and sludge to the boiler. Time slots I–V: I, mono-combustion of wood chips; II, mono-combustion of bark pellets, III, stepwise increase of co-combustion of SRF up to the level corresponding to test case *SRF*; IV, RDF flow corresponding to case *SRF*; V, start of sludge combustion corresponding to *MSS2-high*.

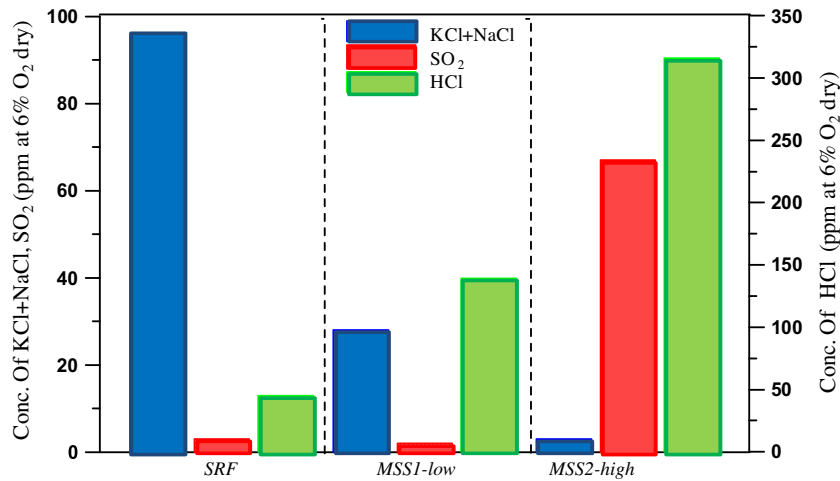


Fig. 5. Concentration of alkali chlorides (KCl + NaCl), HCl and SO₂ before the convection pass (16 in Fig. 1.) recalculated on dry flue gas at 6% O₂.

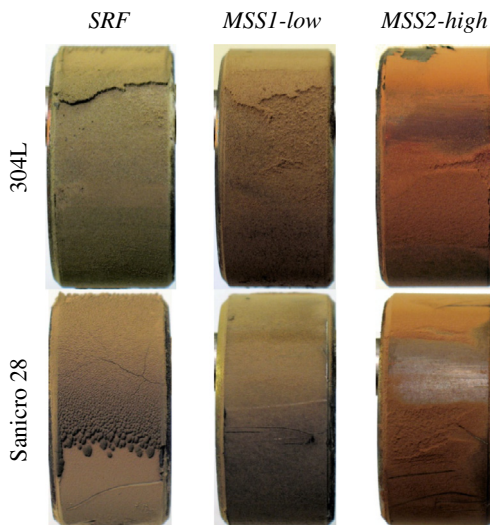


Fig. 6. Optical images of the corrosion probe samples exposed for 24 h at 600 °C.

respectively. However, compared to the SRF case, the presence of sulphate-containing compounds was increased and calcium sulphate (CaSO₄) and K₂Ca₂(SO₄)₃ were detected with medium intensity diffraction peaks. In contrast to SRF and MSS1-low, no alkali chlorides were detected on deposits formed on the MSS2-high sample. Instead, diffraction of high intensity from CaSO₄ and KCaFe(PO₄)₂ and diffractions of medium intensity from K₂Ca₂(SO₄)₃ and KAlSi₂O₆ were detected.

Results from the IC analysis are shown in Fig. 7 which presents the percentage distribution between SO₄²⁻ and Cl⁻ in the deposits. The deposit formed on the SRF sample was dominated by Cl⁻ and just a few percent SO₄²⁻ were detected. The deposit formed on the sample exposed in the MSS1-low case had almost equal distribution between these ions: 47% Cl⁻ and 53% SO₄²⁻. In the MSS2-high case, the deposit was dominated by SO₄²⁻ and the amount of Cl⁻ was less than 2%. In addition to Cl⁻ and SO₄²⁻, the amount of CrO₄²⁻ in the deposit/corrosion products was also detected by IC. In the two exposures where alkali chlorides were detected in the deposit (i.e. SRF and MSS1-low), CrO₄²⁻ was also detected. The amount of CrO₄²⁻ in the SRF case was 150 ppm and 927 ppm in the MSS1-low case. For the MSS2-high case, where the amount of alkali chlorides in the deposit was minimal, the amount of CrO₄²⁻ was below the detection limit of the IC.

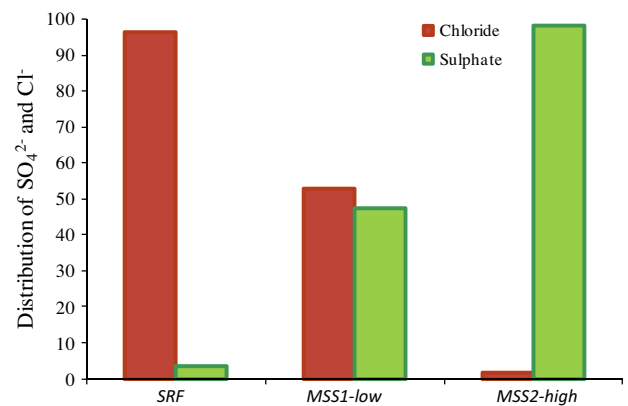


Fig. 7. Percentage distribution between sulfate ions and chloride ions in the deposits formed on the Sanicro 28 samples, exposure cases SRF, MSS1-low and MSS2-high.

3.4. Composition analysis of the deposit/corrosion layer by SEM/EDX

The SEM cross section of the 304L sample exposed for 24 h in the SRF case is shown in Fig. 8. Four distinct areas can be identified in the BSE image. The bright area in the lower section shows the steel sample ring. On top of the ring a somewhat bright corrosion product layer has formed, covered by a greyish deposit layer. Finally, the epoxy can be seen as the black area in the upper part of the image. The thickness of the oxide layer varies between 30 μm and 100 μm, whereas the thickness of the covering deposit layer is 550–600 μm.

Fig. 9 shows maps from the EDX analysis of the selected area (a) in Fig. 8. The results show that the deposit is dominated by Ca. Closest to the corrosion product layer, an area rich in K and Cl can be seen; this can be recognised as KCl with EDX point analysis (also detected with XRD, see Table 4). Other elements that can be detected in the deposit are silica (Si), sodium (Na), P, S and aluminium (Al). The corrosion product layer is divided into two parts: an outer iron-rich oxide (probably present as an outward growing oxide) and an inner oxide rich in iron (Fe), chromium (Cr) and nickel (Ni) (probably present as an inward growing oxide). The outer part is much thicker compared to the inner oxide.

A close-up image of the corrosion product layer is shown in Fig. 10. In the inner part of the oxide scale the density of voids is high. In addition, the 304L sample has suffered from internal

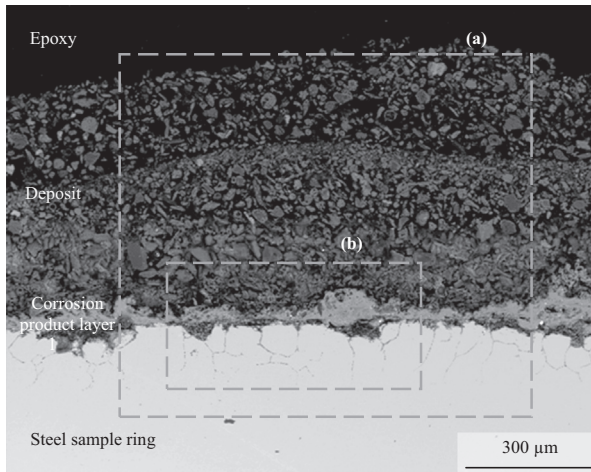


Fig. 8. BSE image of a cross section of the 304L sample exposed in the *SRF* case for 24 h at 600 °C. EDX maps of the selected area (a) are shown in Fig. 9 and a BSE image of the marked area (b) is shown in higher magnification in Fig. 10.

oxidation along the steel grain boundaries. The figure also includes EDX maps for Fe and Cr of the marked area (c). The EDX maps reveals nodules of almost pure chromium oxide (Cr_2O_3) embedded in the outward growing iron-rich oxide.

A SEM image of the cross section of the 304L sample exposed in the *MSSI-low* case is shown in Fig. 11. As in the *SRF* case, four distinct areas can be identified: the steel sample ring, corrosion product layer, deposit layer and epoxy. The oxide thickness is significantly thinner compared to the oxide layer formed in the *SRF* case, being 12–20 μm. The amount of deposit formed on the sample is also less; the thickness of the deposit layer is about 100 μm.

Area (d) in Fig. 11 is shown in higher magnification in Fig. 12. Similar to the oxide layer formed in the *SRF* case, the oxide scale can be divided into two parts: a thicker outer Fe-rich part and a thinner inner Cr-rich part. Below the oxide, voids can be seen and the steel sample ring also shows signs of internal oxidation along the steel grain boundaries. However, the attack is not as severe as in the *SRF* case.

EDX analysis (see Fig. 13) of the area in Fig. 12 shows that the deposit is dominated by K, Ca and S. This is in agreement with

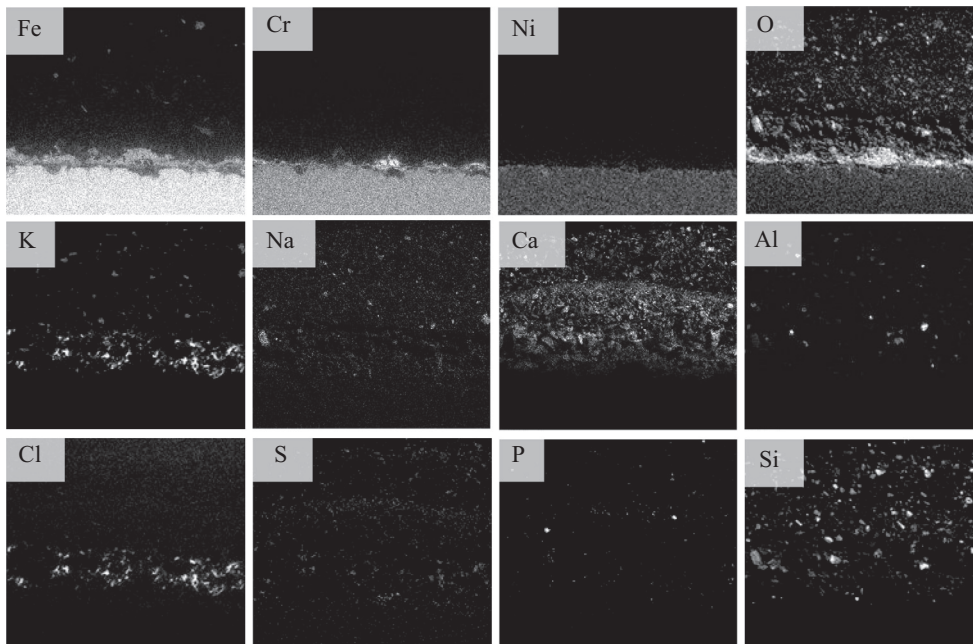


Fig. 9. EDX maps of the selected area (a) in Fig. 8.

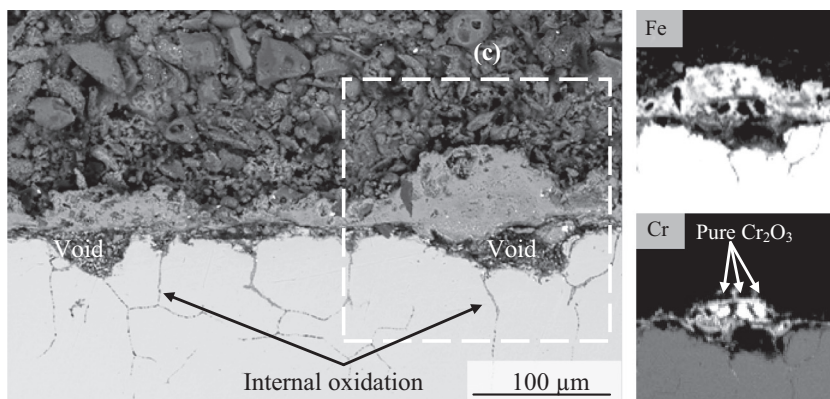


Fig. 10. Left side: BSE image of the marked area “c” in Fig. 8. Right side: EDX maps of the marked area in the left image.

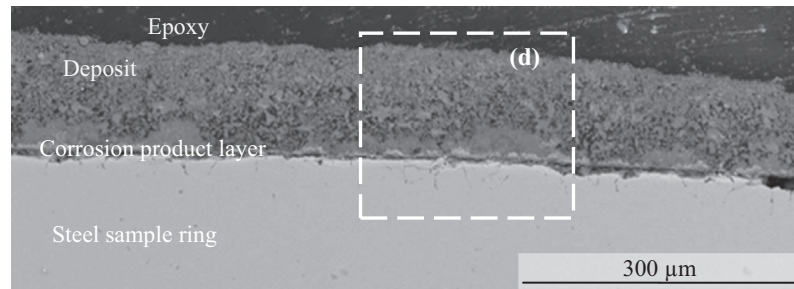


Fig. 11. BSE image of a cross section of the 304L sample exposed in the *MSS1-low* case for 24 h at 600 °C. BSE image of the marked area (d) is shown in higher magnification in Fig. 12.

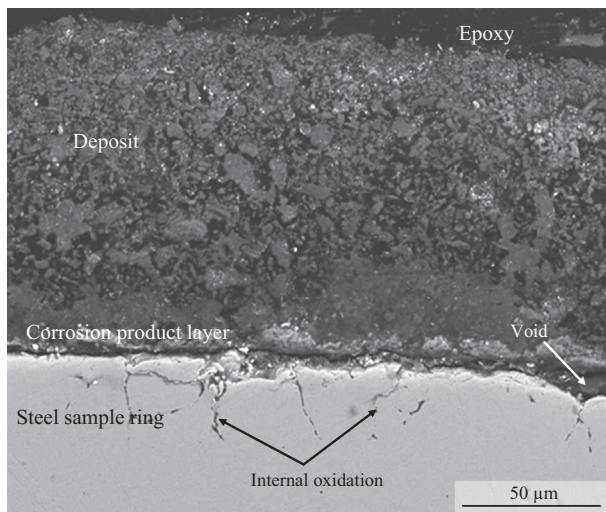


Fig. 12. BSE image of the marked area (d) in Fig. 11.

the XRD analysis (see Table 4) where CaSO_4 and $\text{K}_2\text{Ca}_2(\text{SO}_4)_3$ were detected. High amounts of P can also be seen together with Na, Al and Si. In contrast to the XRD and IC analysis, no Cl could be detected in this part of the deposit.

Fig. 14 shows a SEM cross section of 304L sample exposed in the *MSS2-high* case. In contrast to the *SRF* case and the *MSS1-low* case, no corrosion product layer can be seen between the steel sample ring and the deposit layer. Furthermore, there are no signs of internal oxidation in the steel grain boundaries. The deposit layer is homogenous and consists of a porous network of individual particles, 10–50 μm in size.

A SEM/EDX analysis of the deposit in the *MSS2-high* is shown in Fig. 15. The deposit particles have three varying compositions: Ca, S and oxygen (O); K, C, Fe, P and O; K, Al, Si and O. According to XRD analysis (Table 4), it is proposed that these three different particle compositions are related to the presence of CaSO_4 , $\text{KCaFe}(\text{PO}_4)_2$ and KAlSi_2O_6 .

4. Discussion

The aim of this study was to investigate the effect of co-combusting SRF with digested sewage sludge on the corrosion attack. The steel used for corrosion evaluation in this study is the austenitic stainless steel 304L with 20 wt% Cr and 10 wt% Ni. In a non-corrosive environment, stainless steels withstand high temperature corrosion as it forms a protective oxide consisting of a Cr-rich solid solution, $(\text{Cr,Fe})_2\text{O}_3$. The oxide properties critically depend on its

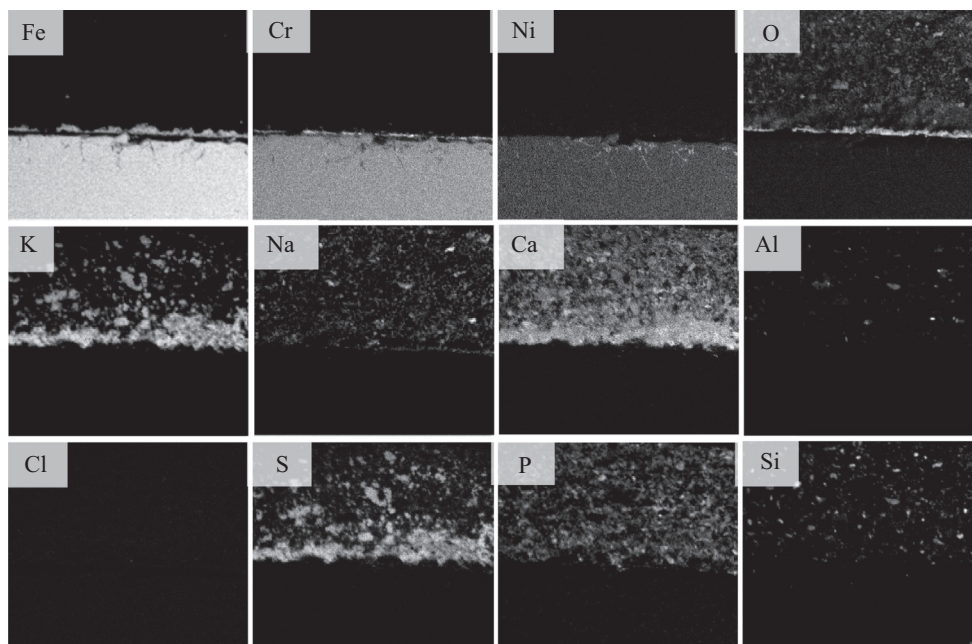


Fig. 13. EDX maps of the area in Fig. 12.

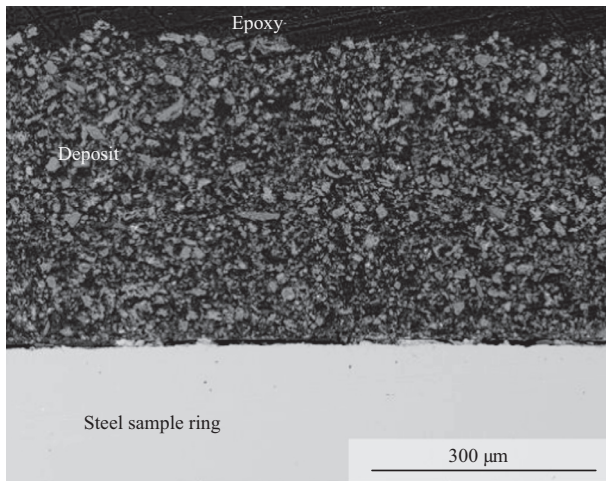
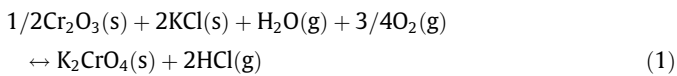
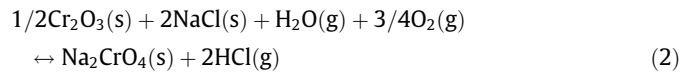


Fig. 14. BSE image of a cross section of the 304L sample exposed in the MSS2-high case for 24 h at 600 °C.

composition, a Cr-rich oxide being protective while a Fe-rich oxide (e.g. pure hematite (Fe_2O_3)) is poorly protective. Hence, all reactions that deplete the oxide in chromia (Cr_2O_3) are potentially harmful. Previous studies in laboratory environments have shown that both water vapour (H_2O) and alkali chlorides (KCl and NaCl) are active in such Cr_2O_3 depleting reactions [7,9,16,35]. In the presence of KCl or NaCl, the Cr_2O_3 depletion is driven by the formation of chromate:

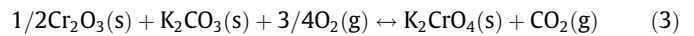


$\Delta G_f^\circ = 74 \text{ kJ/mol}$, $p_{eq}(\text{HCl}) = 1303 \times 10^{-6} \text{ bar}$ (600 °C, p_{O_2} : 0.05 bar, $p_{\text{H}_2\text{O}}$: 0.4 bar) [36] and



$\Delta G_f^\circ = 83 \text{ kJ/mol}$, $p_{eq}(\text{HCl}) = 740 \times 10^{-6} \text{ bar}$ (600 °C, p_{O_2} : 0.05 bar, $p_{\text{H}_2\text{O}}$: 0.4 bar) [36].

If the Cr content drops below a critical level, the oxide loses its protective properties and a rapidly growing (Fe-rich) oxide forms. Therefore, the supply of Cr to the oxide by diffusion in the metal must match the rate of depletion to maintain the protective properties of the oxide. Laboratory exposure on 304L shows that chromate formation results in the fast breakdown of the protective properties of 304L and triggers the formation of an iron-rich scale. In the chromate formation reaction, $\text{HCl}(\text{g})$ is formed. However, during corrosion initiation little or no chlorine have been detected in the corrosion product layer, indicating that the $\text{HCl}(\text{g})$ formed is released to the flue gas [7,9]. Furthermore, 304L exposed in the presence of K_2CO_3 exhibited similar corrosion rate and morphology as for the corresponding exposures in the presence of KCl [18].



$\Delta G_f^\circ = -129 \text{ kJ/mol}$, $p_{eq}(\text{CO}_2) = 5.2 \times 10^6 \text{ bar}$ (600 °C, p_{O_2} : 0.05 bar) [36].

The oxide scale formed as a consequence from reactions (1)–(3) is poorly protective and the corrosion attack may be further accelerated by the inward diffusion e.g. Cl^- and sulphide ions (S^{2-}). In addition, metal chlorides and metal sulphides that form, in the metal/oxide interface are expected to decrease the scale adherence which in turn can lead to the sound metal being exposed to the corrosive flue gases such as HCl and SO_2 [37,38].

In the reference exposure, SRF, the fuel composition was a mixture of 78% bark and 22% SRF. This composition resulted in a flue

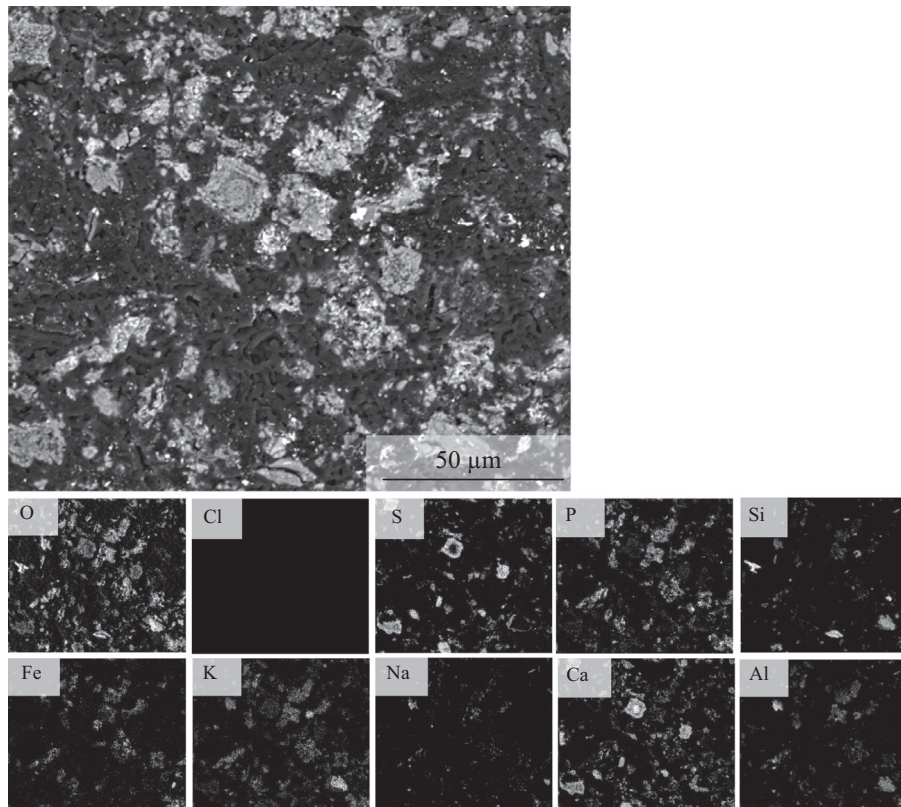
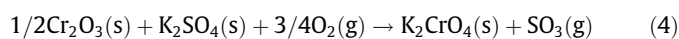


Fig. 15. SEM/EDX analysis of the deposit in Fig. 14.

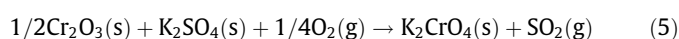
gas containing high levels of gaseous alkali chlorides (96 ppm), measurable levels of HCl(g) (12 ppm) and a low level of SO₂(g) (2 ppm) (see Fig. 5). Accordingly, the deposit formed on the simulated superheater tubes, *i.e.* the corrosion probe, was dominated by alkali chlorides whereas the amount of SO₄²⁻ was very low; only a small percentage of the anions in the deposit was recognised as SO₄²⁻ (see Fig. 7). The alkali chloride-rich deposit in the SRF case gave rise to a severe corrosion attack (Figs. 8 and 10). This corrosion attack is characterised by an oxide scale 30–100 μm thick as well as internal oxidation along the steel grain boundaries and large void formation in the metal/oxide interface. Similar to laboratory exposure with KCl and NaCl on 304L [7,9,17], the oxide scale is divided into two parts: an outer Fe-rich oxide and an inner oxide rich in Fe, Cr and Ni rich oxide (see Fig. 9). By IC analysis, the amount of CrO₄²⁻ detected on the 304L sample exposed in the SRF case was 150 ppm, which is suggested to have formed according to reaction (1) and/or reaction (2). Furthermore, in the Cr map in Fig. 10, nodules of pure Cr oxide can be seen in the outward growing oxide. As 304L forms a solid solution oxide of Fe and Cr when oxidized, this pure Cr₂O₃ is not expected to have been formed from oxidation of the steel. Instead, the nodules of pure Cr oxide are probably the result of decomposition of alkali chromate. The initially formed alkali chromate, formed on the oxide surface, is suggested to decompose to Cr oxide and alkali hydroxide in reducing environments. Nevertheless, Cr has been depleted from the protective oxide initially formed and the Cr₂O₃ nodules are not expected to be protective. Thus, the protective oxide was transformed into a poorly protective and fast growing Fe₂O₃ oxide (detected with XRD, Table 4). Due to this poor protection, the underlying metal can be further attacked and internal oxidation can be clearly seen in Fig. 10.

On the basis of the results presented above, the corrosion attack could be mitigated by minimising the presence of reactive alkali compounds, *e.g.* alkali chlorides. As a consequence, the protective oxide initially formed on the stainless steel remains intact and thus, the corrosion protection of the steel is maintained. Therefore, all reactions where alkali chlorides are converted into less aggressive compounds are beneficial from the point of view of corrosion. Municipal sewage sludge contains high levels of S, P and aluminosilicates, all with the ability to react with alkali chlorides, converting the deposit into less corrosive compounds.

The conversion of alkali chlorides into corresponding alkali sulphates is a successful way of mitigating a corrosion attack. This has been shown in both laboratory exposures [18,39,40] as well as in field exposures by using elemental S, S-rich additives or by co-combustion with a suitable S-rich fuel [15,22,23,26–29]. In contrast to alkali chlorides, K₂SO₄ does not induce an accelerated corrosion attack on 304L steel at this temperature (600 °C). The non-corrosive nature of K₂SO₄ is explained by its relative thermodynamic stability [18,39]. Hence, the reaction of K₂SO₄ with the protective oxide to form K₂CrO₄ is not thermodynamically favoured under the present experimental conditions:



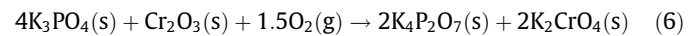
$\Delta G_f^\circ = 135 \text{ kJ/mol}$, $p_{\text{eq}}(\text{SO}_3) = 8.9 \times 10^{-10} \text{ bar}$ (600 °C, p_{O_2} : 0.05 bar) [36].



$\Delta G_f^\circ = 304 \text{ kJ/mol}$, $p_{\text{eq}}(\text{SO}_2) = 6.0 \times 10^{-39} \text{ bar}$ (600 °C, p_{O_2} : 0.05 bar) [36].

Compared to the sulphate chemistry in biomass and waste-fired boilers, the phosphate chemistry is not equally investigated. However, some studies investigating the phosphate chemistry in biomass and waste-fired boilers have been performed in recent years, often in connection to the combustion of Municipal Sewage Sludge (MSS) [41–43]. In these articles, the focus has been on flue

gas and deposit chemistry rather than investigating how phosphorus compounds affect the high temperature corrosion of steels. In fact, little has been published regarding the role of phosphorus compounds and high temperature corrosion. In [44], however, laboratory exposures were performed investigating the effect of different phosphates (Na₂P₂O₇, K₃PO₄ and Ca₂P₂O₇) on stainless steels (Sanicro28 and 304L) at 600–700 °C for 24 h. The study showed that, depending on the type of phosphate (ortho-phosphate compared to pyro-phosphate) and cation (Na, K or Ca), the extent of the corrosion attack was dissimilar. With Ca₂P₂O₇, no accelerated attack was detected compared to the corresponding salt-free exposures. However, for K₃PO₄, and to some extent Na₂P₂O₇, the corrosion attack of the stainless steels was accelerated by the formation of K₂CrO₄, see reaction (6).



$\Delta G_f^\circ = 57 \text{ kJ/mol}$, (600 °C, p_{O_2} : 0.05 bar) [36].

Nevertheless, compared to the corresponding exposures in the presence of KCl, the chromate formation is significantly slower in the presence of alkali phosphates and thus, the corrosion attack is not as severe.

In addition to forming alkali sulphates and alkali phosphates, the MSS has also been suggested to reduce alkali-related problems by converting corrosive alkali chlorides to less corrosive compounds by the reaction with aluminium silicate. The source of alumina silicates in municipal sewage sludge is zeolites, which is a common component in phosphate-free household detergents. Zeolites have a porous structure that can accommodate a wide variety of cations, such as Na⁺, K⁺, Ca²⁺. A previous study shows that the addition of zeolite-rich additives significantly reduced the chlorine and alkali in the deposit [45].

As mentioned, MSS contains high levels of S, P and aluminium silicate, all with the ability to react with alkali chlorides. Hence, the question is to what extent the alkali chlorides are converted by the addition of sewage sludge and secondly, is the conversion dominated by one of these species or are all three at play? Furthermore, how does this affect the corrosion attack on stainless steels?

In exposure case *MSS1-low*, the reference fuel (SRF) was co-combusted with 7.3% municipal sewage sludge. The addition of sludge resulted in a reduction of gaseous alkali chlorides from 96 ppm (case SRF) to 28 ppm. The concentration of HCl increased from 12 ppm to almost 150 ppm while the concentration of SO₂ remained similar. The deposits formed in the SRF case were dominated by alkali chlorides and due to the addition of municipal sewage sludge (*i.e.* *MSS1-low* case) the amount of alkali chlorides in the deposit decreased. According to the results, the decrease in chloride content in the *MSS1-low* case is primarily due to the sulphation (see Table 4, Figs. 7 and 13). However, some of the alkali chlorides have probably been converted into phosphates since there was an increase in phosphorus (compare *MSS1-low* EDX P map in Fig. 13 with SRF EDX P map in Fig. 9). Even though the alkali chlorides were decreased in the deposit, their presence gave rise to the formation of chromates, 970 ppm being detected in the *MSS1-low* case. This value is higher compared to the amount detected on the sample exposed in the SRF case. However, the instability of chromates in reducing atmospheres (*e.g.* beneath oxide scales) may decrease the amount of detectable chromate. It is suggested that the sample exposed in the SRF case had suffered from this effect (see Fig. 10). The extent of the corrosion attack in the sample exposed in the *MSS1-low* decreased compared to the SRF case; the oxide scale is thinner and more even compared to the corresponding exposure in the SRF case, see Fig. 11 and Fig. 12. The oxide scale morphology is however similar, *i.e.* an outward growing Fe-rich oxide and an inward growing oxide containing Fe, Cr and Ni (see Fig. 13). Furthermore, the internal oxidation of the steel is also seen in the *MSS1-low* case but not to the same extent as in the SRF case.

In exposure case *MSS2-high*, the reference fuel (SRF) was co-combusted with 13% municipal sewage sludge. The addition of sludge resulted in the reduction of gaseous alkali chlorides from 96 ppm (case *SRF*) to 3 ppm. The concentration of HCl increased from 12 ppm to 315 ppm and the concentration of SO₂ also increased to 230 ppm. The resulting deposit layer consists of a porous network of individual particles, 10–50 µm in size. The EDX analysis (Fig. 15) reveals that the particles have three types of composition: (1) Ca, S and O (2) K, Ca, Fe, P and O (3) K, Al, Si and O. According to XRD, it is proposed that these compounds are CaSO₄, K₂CaFe(PO₄)₂ and KAlSi₂O₆. In addition, K₂Ca₂(SO₄)₃ was detected by XRD. In contrast to the *SRF* and the *MSS1-low* cases, no alkali chlorides could be detected in the deposit. Furthermore, the lack of chromates detected on the 304L sample indicates that there was no breakdown of the protective oxide. In fact, no corrosion product layer could be seen beneath the deposit layer. Thus, the oxide formed on the sample is in the submicron range, below the resolution of the EDX analysis, probably less than 0.3 µm in thickness. Furthermore, there are no signs of internal oxidation in the steel grain boundaries. The thin oxide formed is expected to be chromium-rich. However, due to its thinness, EDX analysis was not possible.

The protective behaviour of 304L in the *MSS2-high* case shows that the initial corrosion of this stainless steel is much related to the chromate formation, destroying the Cr-rich oxide. If the corrosion attack had been purely chlorine-induced, the corrosion would have also been expected to remain high in the *MSS2-high* case since the conversion of alkali chlorides to alkali sulphates, alkali phosphates and alkali aluminium silicates releases large amounts of HCl(g). The HCl content in the flue gas rises to 12 ppm in the *SRF* case and to 315 ppm in the *MSS2-high* case, see Fig. 4. The deposit layer formed in the *MSS2-high* case is very porous and is expected to be highly permeable towards gas molecules. Thus, if HCl(g) had played a significant role in the initiation of corrosion, the highest corrosion rate would have been expected in *MSS2-high* case.

5. Conclusion

- The Co-combustion of municipal sewage sludge with SRF in a the 12 MW_{th} CFB boiler resulted in a decreased corrosion rate of 304L at 600 °C after 24 h of exposure. Without sewage sludge a thick oxide scale was formed on the samples, covered by a deposit where a large amount of corrosive alkali chlorides was detected.
- The corrosivity of alkali chlorides is attributed to the formation of alkali chromate, formed by the reaction between the protective oxide and the alkali chlorides in the deposit. This results in a poorly protective and fast growing Fe-rich oxide.
- Adding digested sewage sludge to the fuel changes the composition of the deposit and the corrosion rate is significantly decreased. The main reason for this is that alkali chlorides in the deposit are largely replaced by less corrosive alkali sulphates, alkali phosphates and alkali aluminium silicate. In contrast to alkali chlorides, they do not deplete the protective oxide in chromium by forming K₂CrO₄. Additionally, less Cl in the deposit decreases the possibility of formation of transition metal chlorides.

Acknowledgements

This project was financed by Värmeforsk AB (Project A08-817) and by the Swedish Energy Administration. The work was carried out within the High Temperature Corrosion Centre (HTC) together with Energy Conversion, both located at Chalmers University of

Technology. The practical support from the operator at Akademiska Hus AB and the research engineers employed by Chalmers University of Technology is greatly appreciated.

References

- [1] Miles TR, Baxter LL, Bryers RW, Jenkins BM, Oden LL. Boiler deposits from firing biomass fuels. *Biomass Bioenergy* 1996;10(2–3):125–38.
- [2] Jenkins BM, Baxter LL, Miles TR. Combustion properties of biomass. *Fuel Process Technol* 1998;54(1–3):17–46.
- [3] Davidsson KO, Åmand L-E, Leckner B, Kovacevic B, Svane M, Hagström M, et al. Potassium, chlorine, and sulfur in ash, particles, deposits, and corrosion during wood combustion in a circulating fluidized-bed boiler. *Energy Fuels* 2007;21(1):71–81.
- [4] Aho M, Paakkinen K, Taipale R. Quality of deposits during grate combustion of corn stover and wood chip blends. *Fuel* 2013;104:476–87.
- [5] Grabke HJ, Reese E, Spiegel M. The effects of chlorides, hydrogen chloride, and sulfur dioxide in the oxidation of steels below deposits. *Corros Sci* 1995;37(7):1023–43.
- [6] Jonsson T, Froitzheim J, Pettersson J, Svensson J-E, Johansson L-G, Halvarsson M. The influence of KCl on the corrosion of an austenitic stainless steel (304L) in oxidizing humid conditions at 600 °C: a microstructural study. *Oxid Met* 2009;73(3–4):213–39.
- [7] Karlsson S, Pettersson J, Johansson L-G, Svensson J-E. Alkali induced high temperature corrosion of stainless steel – the influence of NaCl, KCl and CaCl₂. *Oxid Metals* 2012;78(1–2):83–102.
- [8] Pettersson C, Pettersson J, Asteman H, Svensson J-E, Johansson L-G. KCl-induced high temperature corrosion of the austenitic Fe–Cr–Ni alloys 304L and Sanicro 28 at 600 °C. *Corros Sci* 2006;48(6):1368–78.
- [9] Pettersson J, Asteman H, Svensson J-E, Johansson L-G. KCl induced corrosion of a 304-type austenitic stainless steel at 600 °C; the role of potassium. *Oxid Metals* 2005;64(1–2):23–41.
- [10] Pettersson J, Svensson J-E, Johansson L-G. KCl-induced corrosion of a 304-type austenitic stainless steel in O-2 and in O-2 + H₂O environment: the influence of temperature. *Oxid Metals* 2009;72(3–4):159–77.
- [11] Pickering H, Beck F, Fontana M. Rapid intergranular oxidation of 18–8 stainless steel by oxygen and dry sodium chloride at elevated temperatures. *Trans ASM* 1961;53:793–803.
- [12] Nielsen HP, Frandsen FJ, Dam-Johansen K, Baxter LL. The implications of chlorine-associated corrosion on the operation of biomass-fired boilers. *Prog Energy Combust Sci* 2000;26(3):283–98.
- [13] Shinata Y. Accelerated oxidation rate of chromium induced by sodium chloride. *Oxid Metals* 1987;27(5–6):315–32.
- [14] Wang C-J, He T-T. Morphological development of subscale formation in Fe–Cr–(Ni) alloys with chloride and sulphates coating. *Oxid Metals* 2002;58(3–4):415–37.
- [15] Pettersson J, Pettersson C, Folkesson N, Johansson L-G, Skog E, Svensson J-E. The influence of sulphur additions on the corrosive environment in a waste-fired CFB boiler. *Mater Sci Forum* 2006;522–523:563–70.
- [16] Lehmusto J, Skrifvars B-J, Yrjas P, Hupa M. Comparison of potassium chloride and potassium carbonate with respect to their tendency to cause high temperature corrosion of stainless 304L steel. *Fuel Process Technol* 2013;105:98–105.
- [17] Proff C, Jonsson T, Pettersson C, Svensson J-E, Johansson L-G, Halvarsson M. Microstructural investigation of the KCl-induced corrosion of the austenitic alloy Sanicro 28 (³⁵Fe²⁷Cr³¹Ni) at 600 °C. *Mater High Temp* 2009;26(2):113–25.
- [18] Pettersson J, Folkesson N, Svensson JE, Johansson LG. The effects of KCl, K₂SO₄ and K₂CO₃ on the high temperature corrosion of a 304-type austenitic stainless steel. *Oxid Metals* 2011;76(1–2):93–109.
- [19] McNallan MJ, Liang WW, Kim SH, Kang CT. Acceleration of the high temperature oxidation of metals by chlorine. In: *High temperature corrosion*. NACE 1983;1:316–21.
- [20] Lee YY, McNallan MJ. Ignition of nickel in environments containing oxygen and chlorine. *Metall Trans A* 1987;18(13):1099–107.
- [21] Aho M, Yrjas P, Taipale R, Hupa M, Silvennoinen J. Reduction of superheater corrosion by co-firing risky biomass with sewage sludge. *Fuel* 2010;89(9):2376–86.
- [22] Folkesson N, Pettersson J, Pettersson C, Johansson L-G, Skog E, Andersson B-Å, et al. Fireside corrosion of stainless and low alloyed steels in a waste-fires CFB boiler: the effect of adding sulphur to the fuel. *Mater Sci forum* 2008;595–598:289–97.
- [23] Jonsson T, Pettersson J, Davidsson K, Johansson LG, Svensson JE. Sewage sludge as additive to reduce the initial fireside corrosion caused by combustion of shredder residues in a waste-fired BFB boiler. In: 9th Liège conference on materials for advanced power engineering; 2010.
- [24] Davidsson KO, Åmand L-E, Steenari B-M, Elled A-L, Eskilsson D, Leckner B. Countermeasures against alkali-related problems during combustion of biomass in a circulating fluidized bed boiler. *Chem Eng Sci* 2008;63(21):5314–29.
- [25] Kassman H, Bäfver L, Åmand L-E. The importance of SO₂ and SO₃ for sulphation of gaseous KCl – an experimental investigation in a biomass fired CFB boiler. *Combust Flame* 2010;157(9):1649–57.

- [26] Kassman H, Pettersson J, Steenari B-M, Åmand L-E. Two strategies to reduce gaseous KCl and chlorine in deposits during biomass combustion – injection of ammonium sulphate and co-combustion with peat. *Fuel Process Technol* 2013;105:170–80.
- [27] Andersson S, Blomqvist EW, Bäfver L, Jones F, Davidsson K, Froitzheim J, et al. Sulfur recirculation for increased electricity production in waste-to-energy plants. *Waste Manage* 2014;34(1):67–78.
- [28] Krause HH, Vaughan DA, Boyd WK. Corrosion and deposits from combustion of solid waste—Part III: effects of sulfur on boiler tube metals. *J Eng Power* 1975;97(3):448–52.
- [29] Viklund P, Pettersson R, Hjärnhede A. Effect of sulphur containing additive on initial corrosion of superheater tubes in waste fired boiler. *Corros Eng Sci Technol* 2009;44(3):234–40.
- [30] Vainio E, Yrjas P, Zevenhoven M, Brink A, Laurén T, Hupa M, et al. The fate of chlorine, sulfur, and potassium during co-combustion of bark, sludge, and solid recovered fuel in an industrial scale BFB boiler. *Fuel Process Technol* 2013;105:59–68.
- [31] Elled A-L, Davidsson K-O, Åmand L-E. Sewage sludge as a deposit inhibitor when co-fired with high potassium fuels. *Biomass Bioenergy* 2010;34:1546–54.
- [32] Åmand L-E, Leckner B, Eskilsson D, Tullin C. Ash deposition on heat transfer tubes during combustion of demolition wood. *Energy Fuels* 2006;20:1001–7.
- [33] Davidsson K-O, Åmand L-E, Elled A-L, Leckner B. Effect of cofiring coal and biofuel with sewage sludge on alkali problems in a circulating fluidized bed boiler. *Energy Fuels* 2007;21:3180–8.
- [34] Wang L, Hustad JE, Skreiberg Ø, Skjevraak G, Grønli M. A critical review on additives to reduce ash related operation problems in biomass combustion applications. *Energy Proc* 2012;20:20–9.
- [35] Asteman H, Svensson JE, Johansson LG, Norell M. Indication of chromium oxide hydroxide evaporation during oxidation of 304L at 873 K in the presence of 10% water vapor. *Oxid Metals* 1999;52(1–2):95–111.
- [36] Barin I. *Thermodynamic data of pure substances*, 3rd ed.. New York: Weinheim; 1995. p. 1885.
- [37] Folkesson N, Johansson LG, Svensson JE. Initial stages of the HCl-induced high-temperature corrosion of alloy 310. *J Electrochem Soc* 2007;154(9):515–21.
- [38] Jonsson T, Folkesson T, Svensson J-E, Johansson L-G. An ESEM in-situ investigation of initial stages of the KCl induced high temperature corrosion of a Fe–2.25Cr–1Mo steel at 400 °C. *Corros Sci* 2011;53(3):2233–46.
- [39] Karlsson S, Pettersson J, Svensson J-E, Johansson L-G. KCl-induced high temperature corrosion of austenitic stainless steel 304L – the influence of SO₂. *Mater Sci Forum* 2011;696:224–9.
- [40] Skrifvars BJ, Backman R, Hupa M, Salmenoja K, Vakkilainen E. Corrosion of superheater steel materials under alkali salt deposits Part 1: the effect of salt deposit composition and temperature. *Corros Sci* 2008;50(5):1274–82.
- [41] Skoglund n, Grimm A, Öhman M, Boström D. Combustion of biosolids in a bubbling fluidized bed, Part 1: main ash-forming elements and ash distribution with a focus on phosphorus. *Energy Fuels* 2014;28(2):1183–90.
- [42] Li L, Ren Q, Li S, Lu Q. Effect of phosphorus on the behavior of potassium during the co-combustion of wheat straw with municipal sewage sludge. *Energy Fuels* 2013;27(10):5923–30.
- [43] Elled A-L, Åmand L-E, Leckner B, Andersson B-Å. Influence of phosphorus on sulphur capture during co-firing of sewage sludge with wood or bark in a fluidised bed. *Fuel* 2006;85(12–13):1671–8.
- [44] Herstad Svärd S, Åmand LE, Bowalli J, Öhlin J, Steenari BM, Pettersson J, et al. Frame work – measures for simultaneous minimization of alkali related operating problems, phase 3 Värmeforsk, Göteborg, Sweden; 2011.
- [45] Pettersson A, Elled AE, Möller A, Steenari BM, Åmand LE. The impact of zeolites during co-combustion of municipal sewage sludge with alkali and chlorine rich fuels. In: *The 20th international conference on fluidized bed combustion*. Berlin Heidelberg. Xi'an, China: Springer; 2009.